metals

MDPI

Article

Smoothed-Particle Hydrodynamics (SPH) Simulation of AA6061-AA5086 Dissimilar Friction Stir Welding

Hamed Jamshidi Aval

Department of Materials Engineering, Babol Noshirvani University of Technology, Shariati Avenue, Babol 47148-71167, Iran; h.jamshidi@nit.ac.ir; Tel.: +98-11-35501808; Fax: +98-11-35501802

Abstract: The present study investigates thermo-mechanical issues associated with the dissimilar friction stir welding process of AA6061 and AA5086 aluminum alloys through smoothed-particle hydrodynamics (SPH) simulation and experimental investigations. The results demonstrate that the presented model accurately predicts the thermal history during the friction stir welding process. Furthermore, both simulation and experimental data indicate that when the AA6061 alloy is located on the advancing side, the temperature profile is drawn towards the AA6061 alloy. Conversely, the temperature profile is more symmetrical when the AA6061 alloy is positioned on the retreating side. Additionally, simulation results reveal that when the AA5086 alloy is on the advancing side, the strain rate distribution between the advancing and retreating sides is nearly symmetrical. When the AA5086 alloy is placed on the advancing side, the temperature and strain rate on the advancing side are higher than on the retreating side, compared to when the AA5086 alloy is located on the retreating side.

Keywords: smoothed-particle hydrodynamics; thermo-mechanical simulation; dissimilar FSW; aluminum alloys

check for updates

Citation: Jamshidi Aval, H. Smoothed-Particle Hydrodynamics (SPH) Simulation of AA6061-AA5086 Dissimilar Friction Stir Welding. *Metals* **2023**, *13*, 906. https://doi.org/10.3390/met13050906

Academic Editor: Miguel Cervera

Received: 2 April 2023
Revised: 1 May 2023
Accepted: 6 May 2023
Published: 7 May 2023

Copyright: © 2023 by the author. Licensee MDPI, Basel, Switzerland. This article is an open access article distributed under the terms and conditions of the Creative Commons Attribution (CC BY) license (https://creativecommons.org/licenses/by/4.0/).

1. Introduction

Friction stir welding (FSW) is a versatile process used for welding similar and dissimilar metals [1]. It has many applications, especially in joining AA5xxx and AA6xxx series aluminum alloys, which have poor weldability with fusion welding processes. It is also helpful in joining AA2xxx and AA7xxx series aluminum alloys, which cannot be joined using fusion processes. In contrast to fusion processes, FSW is a solid-state welding process and thus does not produce defects caused by the solidification of the weld metal. While FSW is economically justified under conditions of high production rates, its high initial investment cost limits its application [2]. It was found that the mechanical and microstructural properties of friction stir welded samples could be a function of several variables, including welding process parameters and external boundary conditions such as rotational and welding speed, geometric parameters of the tool and the workpiece, and the initial temperature of the material.

Extensive research has been conducted on FSW due to its ability to weld dissimilar aluminum alloys to each other and non-ferrous materials to ferrous materials, such as aluminum to steel. These studies have led to the extensive development of the FSW process in the aerospace and automotive industries.

The FSW process is widely used for joining aluminum alloys in various industries, including automobiles, shipbuilding, railway, aviation, and the military [3]. Controlling welding parameters is necessary to achieve desirable properties during FSW. Welding parameters affect various factors, such as temperature distribution, weld cooling rate, weld microstructure, and residual stress distribution. This has led to an increasing tendency to analyze heat transfer and plastic deformation phenomena quantitatively [4].

Experimental studies in this field are limited to temperature measurement, microstructural studies, mechanical evaluation, and measurement of residual stress distribution [5,6]. These methods are time consuming, expensive, and cannot accurately check parameters such as strain rate and material flow. Hence, numerical modeling concepts have become more relevant and systematic in explaining the phenomena that occur during FSW and in investigating how welding parameters affect the quality of the weld. In recent years, quantitative analysis of heat transfer and plastic deformation phenomena in weld nuggets has gained popularity. This has enabled researchers to relate process conditions to the quality of the weldments and to optimize the welding process.

Theoretical models provide a powerful tool to check the physical concepts of the welding process, estimate important input parameters, and calculate the effects of changing any parameter. Thus, numerical modeling has become essential for understanding the FSW process and optimizing its parameters to achieve the desired results [7,8].

Numerical modeling has become a valuable tool in understanding and optimizing the FSW process. Over the years, numerous numerical models have been developed in this field [9–11]. For example, Nandan et al. [12] developed a computational fluid dynamics (CFD) model to obtain the temperature distribution and plastic flow during FSW. Similarly, Arora et al. [13] presented a method for measuring plastic strain and strain rate during FSW, based on a CFD model. Chen et al. [14] proposed a new frictional boundary condition at the tool/workpiece interface using the Coulomb friction model for CFD modeling of FSW.

Using a 3D CFD model, Shi et al. [15] quantitatively analyzed the effect of the welding parameters and tool geometry on the thermal history and tool torque in reverse dual rotation friction stir welding. Additionally, Chen et al. [16] used a CFD-based numerical simulation method to analyze the pinning effect on material flow in the FSW process. Employing a 3D transient computational fluid dynamics model, Sun and Wu [17] investigated the effect of the pin on the material flow and thermal history in FSW.

Zhang et al. [18] integrated a geometric model with a CFD model to investigate the effects of the tool tilt angle on heat and mass transfer in the FSW process. Furthermore, Yang et al. [19] developed a CFD model for the numerical simulation of heat and mass transfer and material mixing in FSW of aluminum and magnesium alloys. In another study, Yang [20] proposed a numerical method to predict heat input during FSW, to reduce the effect of heat-induced defects.

Recently, Xiao et al. [21] presented a smoothed-particle hydrodynamics (SPH) method for numerical heat transfer analysis during the FSW process. This method has shown potential for accurate and efficient numerical modeling of the FSW process.

Despite the widespread application of the FSW process in various industries, its physics remains unclear due to its complexity. Effective and reliable models can significantly help to unravel the physical processes during FSW. The development of FSW process modeling methods is still ongoing, and many studies have been conducted to provide a complete model of the process.

This research primarily aimed to provide a thermo-mechanical model for dissimilar FSW welding of AA5086 and AA6061 aluminum alloys. Accordingly, the temperature distribution and material flow in the welding process were predicted using the SPH method. The heat transfer and plastic deformation equations were simultaneously solved to accurately predict temperature distribution and material flow during welding.

2. Simulation of FSW

The SPH method was utilized to simulate the FSW process using the ABAQUS 6.12 software (Johnston, RI, USA). Meshless methods generally do not require a grid for solving problems governed by partial differential equations with various boundary conditions. In conventional mesh-based methods, large deformations can lead to the distortion of elements and a loss in desired accuracy. Re-meshing solutions have been proposed to overcome this issue, but they can only be applied to two-dimensional problems and require complex and strong mesh construction methods. Creating hexahedral elements for 3D

problems presents further difficulties, prompting researchers to develop meshless methods to avoid such problems.

The SPH method is a meshless method that utilizes function approximation to discretize equations and applies a unique solution process. It has gained the attention of many researchers and has become a valuable tool in numerical simulations of various physical processes, including FSW.

Computational fluid dynamics (CFD)-based simulations are usually used to describe large material deformations and to model the mixing action. As in other Eulerian-based discretization schemes, incorporating cell quantities such as temperature-dependent viscosity, that vary by several orders of magnitude, poses a massive challenge to fluid-based simulation approaches. In addition, Eulerian-based CFD models usually produce an unrealistically large tool-influenced zone due to their inability to model the behavior of fluids with large viscosity variations.

An alternative approach to modeling complex industrial flows is using Lagrangian particle-based methods such as SPH. Despite its name ("hydrodynamics"), SPH has been extensively used in solid mechanics applications, particularly for modeling crack propagation and formation. Because of its Lagrangian particle nature, SPH has several advantages for modeling processes involving large material deformations and complex heat flows: (i) complex interface and free surface flows/deformations, including material coalescence and splitting, can be modeled without significant computational efforts; (ii) since the momentum conservation equation does not contain a non-linear term in the Lagrangian framework, SPH can provide an accurate solution for momentum-dominated flows; (iii) it is easy to implement coupled, complicated physics such as realistic equations of state, melting/solidification (near-surface overheating), heat generation resulting from viscous dissipation and latent heat generation, strain and strain rate histories, stick–slip conditions at the tool interface, fracturing, void formation, electrodynamics, chemistry, and history dependence of material properties. In addition, SPH simulations explicitly conserve mass, momentum, and energy. The moving particles not only track the interface but are also used to solve governing differential equations. Furthermore, the SPH method is manifestly Galilean invariant, because particle–particle interactions depend on relative particle positions and velocity differences. The number of particles needed in SPH simulations is determined only by the required resolution and accuracy of the numerical solutions of the macroscopic governing equations.

The two base metals were treated as non-Newtonian fluids in this study's simulation process. The Navier–Stokes equations governing the conservation of mass, energy, and momentum can be defined as follows:

$$\frac{d\rho}{dt} = -\rho\,\nabla\cdot V \tag{1}$$

$$\frac{dV}{dt} = -\frac{\nabla P}{\rho} + \frac{\nabla.\sigma}{\rho} \tag{2}$$

$$\rho c_p \frac{\partial T}{\partial t} = \frac{\partial}{\partial x}\left[k\frac{\partial T}{\partial x}\right] + \frac{\partial}{\partial y}\left[k\frac{\partial T}{\partial y}\right] + \frac{\partial}{\partial z}\left[k\frac{\partial T}{\partial z}\right] + \dot{Q} \tag{3}$$

where ρ represents the material's density, c_p represents the material's heat capacity, k is the material's thermal conductivity, T is the material's temperature, t is the simulation time, and $\dot{Q}$ is the heat generation rate per unit volume. The value of $\dot{Q}$. can be calculated using the following equation [22]:

$$\dot{Q} = \eta S_{ij}\dot{\varepsilon}_{ij}^{pl} \tag{4}$$

where η represents the fraction of plastic energy converted into heat, S_{ij} is the shear stress tensor, and $\dot{\varepsilon}_{ij}^{pl}$ is the plastic strain rate tensor. For this study, it was assumed that 90% of the plastic energy is converted into heat.

The governing equations were discretized using the meshless SPH method, which uses separate sets of points or particles to discretize the welded materials, welding tool, and backing plate. Boundary conditions related to the interface of the tool/workpiece, including the interface of the tool shoulder with the workpiece and the pin with the workpiece, were considered, and the heat transfer between them was calculated using the following equation [12]:

$$k\frac{\partial T}{\partial n}\,|_{S,P} = q_{surf} \tag{5}$$

where q_{surf} represents the heat produced at the interface between the tool and the workpiece. The value of q_{surf} can be calculated as follows:

$$q_{surf} = \mu p \dot{\gamma} \tag{6}$$

where μ represents the friction coefficient, p stands for pressure, and $\dot{\gamma}$ denotes the sliding rate.

The heat transfer coefficient between the tool shoulder and the workpiece was considered to be 10,000 W/m^2 °C. Additionally, it was assumed that 100% of the frictional work is converted into heat, and 90% of the generated heat is transferred to the workpiece. One limitation of current research is the unavailability of comprehensive information about the friction coefficient. The friction coefficient in the current model is a function of the temperature, pressure, and sliding rate. The data used for these variables can be found in [23,24].

The boundary conditions on the surfaces of the tool and workpiece are considered as follows [12]:

$$k\frac{\partial T}{\partial n}\,|_{\Gamma} = h(T - T_0) \tag{7}$$

where n is the normal vector on the boundary Γ and h is the convection coefficient. In the calculations, the convection coefficient is considered to be 20 W/m^2 °C. For ease of modeling, the surface of the workpiece in contact with the backing plate, the contact surfaces of the workpiece with the holders, and the surface of the tool in contact with the FSW machine are assumed to have convection heat transfer, with an effective convection coefficient expressed as follows:

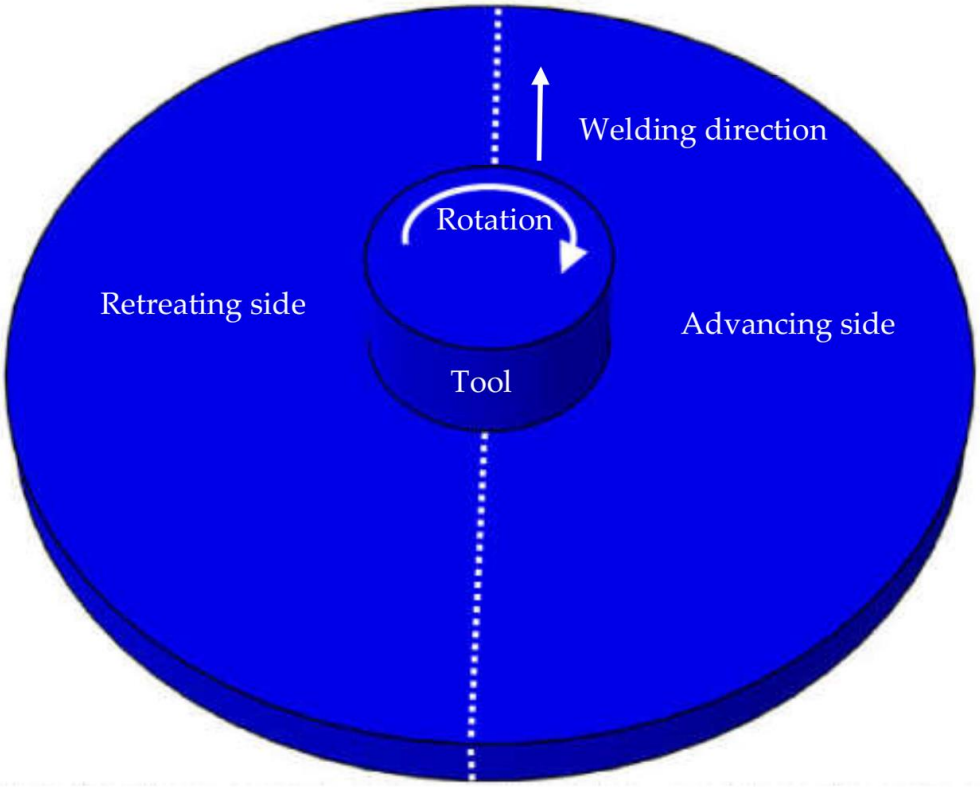
$$k\frac{\partial T}{\partial n}\,|_{\Gamma} = h_e(T - T_0) \tag{8}$$

The study considered an effective convection coefficient of 1000 W/m^2 °C while assuming an initial temperature of 20 °C for both the workpiece and tool. In order to optimize the solution time, only a portion of the workpiece was analyzed, represented by a 100 mm diameter disk, as depicted in Figure 1.

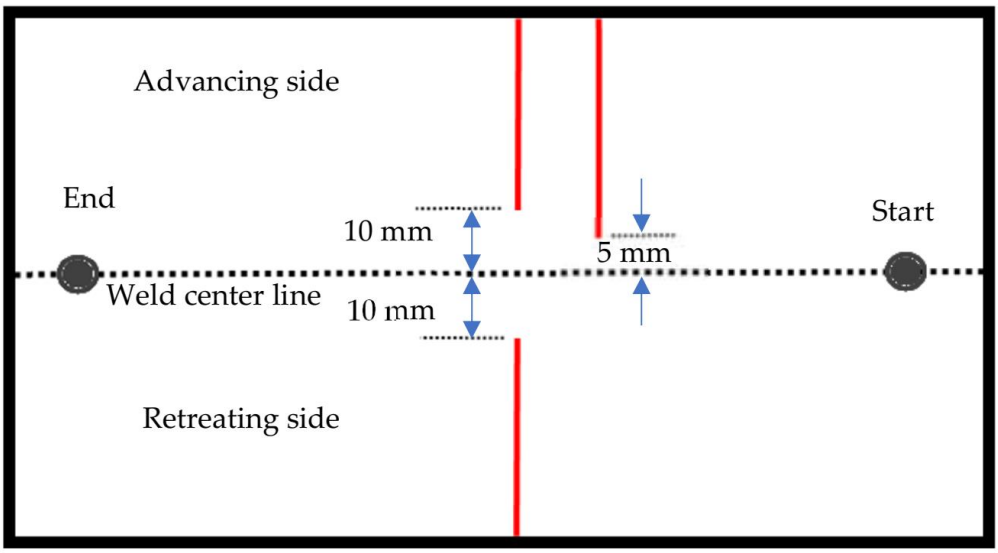
The workpieces were composed of 567,456 particles, and the physical properties of the aluminum alloys AA5086 and AA6061 were extracted from [25,26]. The workpiece deformation behavior was simulated using the Johnson–Cook equation, which is expressed as follows:

$$\sigma_y = (1 - D)[A + B(1 - D)\varepsilon_P^n]\left[1 + C\ln\left((1 - D)\frac{\dot{\varepsilon}_P}{\dot{\varepsilon}_0}\right)\right]\left[1 - \left(\frac{T - T_h}{T_s - T_h}\right)^m\right] \tag{9}$$

The Johnson–Cook equation constant can be found in [27,28]. For the simulation, a reference strain rate ($\dot{\varepsilon}_0$) of 1 s^{-1} was assumed. Additionally, the Johnson–Cook equation factored in the damage value (D), which was calculated using the methodology outlined in [29,30].



(**a**)



(**b**)

Figure 1. (**a**) The domain used in the simulation process, (**b**) schematic view of the thermocouple's positions.

3. Experimental Procedure

This research utilized 4 mm thick sheets of AA5086 and AA6061 aluminum for testing. Tables 1 and 2 present the alloys' chemical compositions and mechanical properties. The AA5086 alloy sheets were in the annealed condition, while the AA6061 alloy sheets were in the T6 condition. The sheets were cut into 15 × 5 cm^2 dimensions and welded by a cylindrical pin tool with a diameter of 5 mm and height of 3.9 mm in an FSW machine via the position control methodology. The tool was positioned at a 3° tilt angle. The welding process was conducted at a rotational speed of 900 rpm and a traverse speed of 10 and 15 cm/min. The ambient temperature during welding was 25 °C. The resulting samples were named according to Table 3. During welding, temperature measurements were taken at various positions via K-type thermocouples. The thermal history during and after FSW was also experimentally measured using K-type thermocouples of 1.5 mm diameter. The temperature history of welded samples in various regions was measured by inserting two thermocouples on the advancing side at a distance of 5 and 10 mm from the weld line and one thermocouple on the retreating side at a distance of 10 mm from the weld line, as shown in Figure 1b. After welding, the samples were cut perpendicular to the welding direction to examine the microstructure of the weld zone, and cross-sections were prepared using metallographic techniques. Poulton and Keller's etchants were used to reveal the microstructures of the AA6061 and AA5086 sides, respectively. The residual stress of the welded samples was measured through the X-ray method. The residual stress measurements were carried out using Cr Ka radiation with the X-ray tube operating at 20 kV and a 4 mA target current. The Vickers micro-hardness test was carried out to determine the hardness profile of different joints and to characterize the hardness profile on the cross-section of the welded samples perpendicular to the weld line at 2 mm from the weld root, using a 100 gf load and a holding time of 15 s.

Table 1. Chemical compositions of the AA5086 and AA6061 alloys.

Alloy	Mg	Mn	Cu	Cr	Si	Fe	Al
AA5086	3.98	0.51	0.016	0.15	0.26	0.28	Bal.
AA6061	0.97	0.045	0.328	0.08	0.52	0.41	Bal.

Table 2. The mechanical properties of the AA5086 and AA6061 alloys.

Alloy	Yield Strength (MPa)	Ultimate Tensile Strength (MPa)	Elongation (%)
AA5086	112 ± 5	253 ± 10	26 ± 3
AA6061	278 ± 7	315 ± 15	10 ± 2

Table 3. The welded samples labelling.

Sample	Rotational Speed (rpm)	Traverse Speed (cm/min)	Advancing Side	Retreating Side
S1	1000	10	AA5086	AA6061
S2	1000	20	AA5086	AA6061
S3	1000	10	AA6061	AA5086
S4	1000	20	AA6061	AA5086

4. Results and Discussion

Figure 2 compares the temperature profiles of samples S1, S2, S3, and S4 after 15 s of welding. S1 and S3 were welded at a rotational speed of 900 rpm and a traverse speed of 10 cm/min. The difference between these two joints was the placement of the AA5086 and AA6061 alloys. Specifically, the AA5086 alloy was on the advancing side in S1 and the retreating side in S3. When positioned on the advancing side, the temperature profile shifted towards the AA6061 alloy. Conversely, when the AA6061 alloy was placed on the retreating side, the temperature profile became more symmetrical than in the previous state.

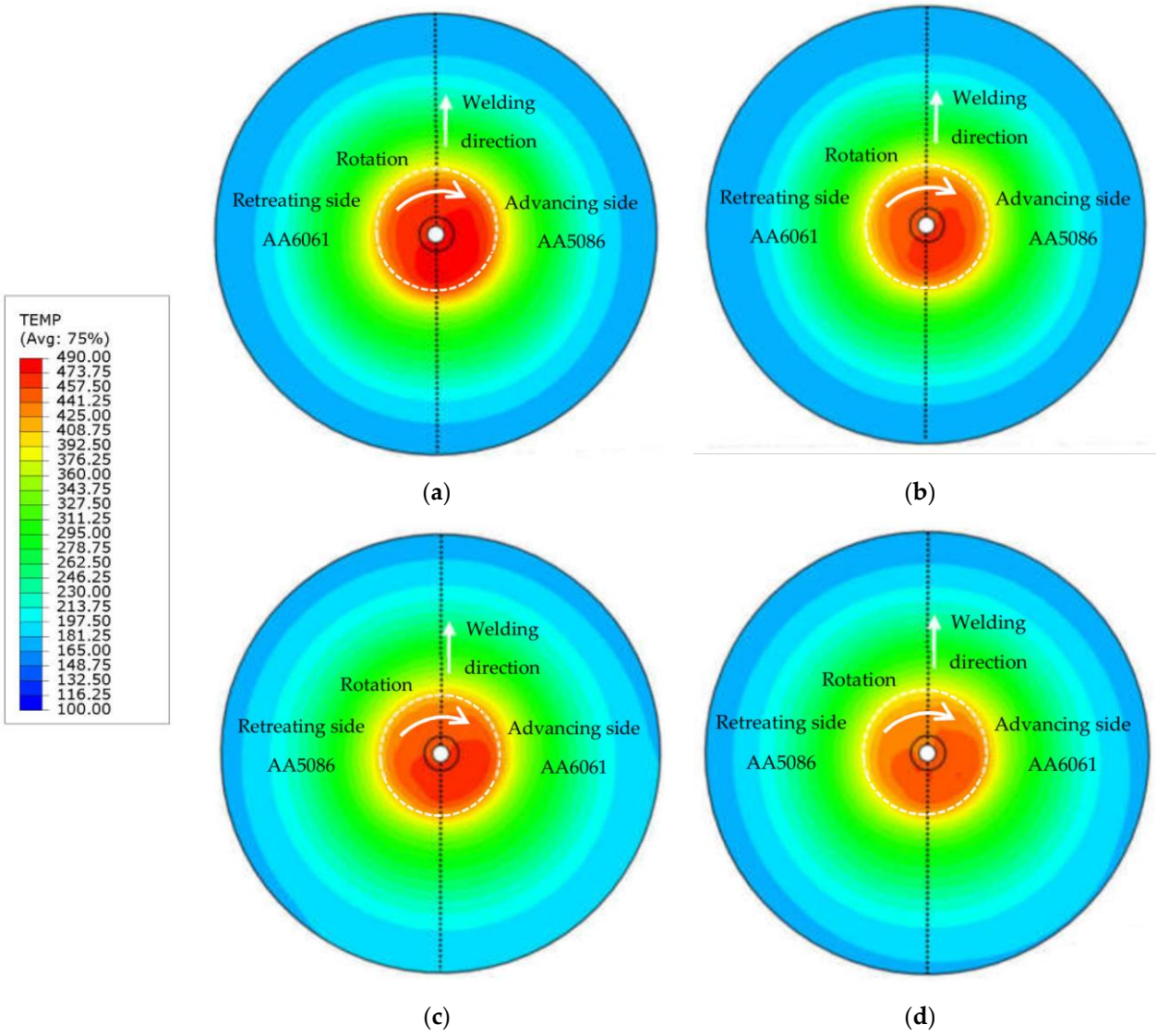


Figure 2. The temperature profile of: (**a**) sample S1, (**b**) sample S2, (**c**) sample S3, (**d**) sample S4. The tool position is marked by the white dashed line.

A similar trend was observed for samples S2 and S4. This could be due to the asymmetric nature of the FSW process and the higher thermal diffusivity of the AA6061 alloy compared to the AA5086 alloy, particularly since the thermal diffusivity of the AA6061 alloy demonstrated a greater increase with increasing temperature relative to the AA5086 alloy. By increasing the temperature from 25 to 500 °C, the thermal diffusivity of AA5086 increases from 0.531 to 0.572 $cm^2 \cdot s^{-1}$. Furthermore, the thermal diffusivity of AA6061 increases from 0.690 to 0.752 $cm^2 \cdot s^{-1}$ when the temperature is increased from 25 to 500 °C [25,26]. Figure 3 depicts the experimental measurement of the temperature profile for the welding of samples S1 and S3. This figure highlights a temperature difference of 25 °C in sample S3 between the advancing and retreating sides, compared to a temperature difference of 12 °C in sample S1 at a distance of 10 mm from the welding center line. This phenomenon confirms the temperature profile deviation towards the AA6061 alloy, as observed in the simulation. Additionally, the thermal cycle on the advancing side was wider when the AA6061 alloy was placed on the advancing side. Moreover, the thermal cycle showed a similar cooling and heating rate on both sides when the AA5086 alloy was located on the advancing side, indicating a relatively symmetrical temperature profile on these two sides. This observation confirms the simulation results (Figure 2).

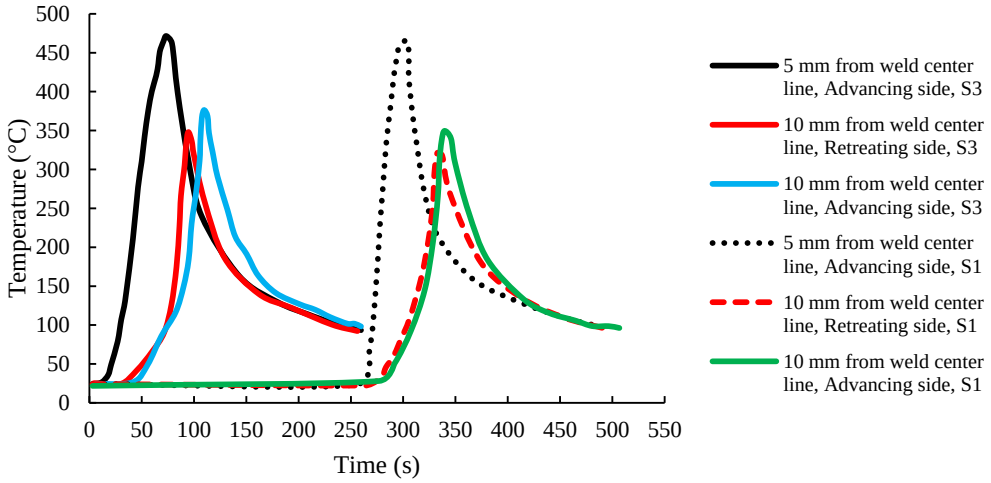
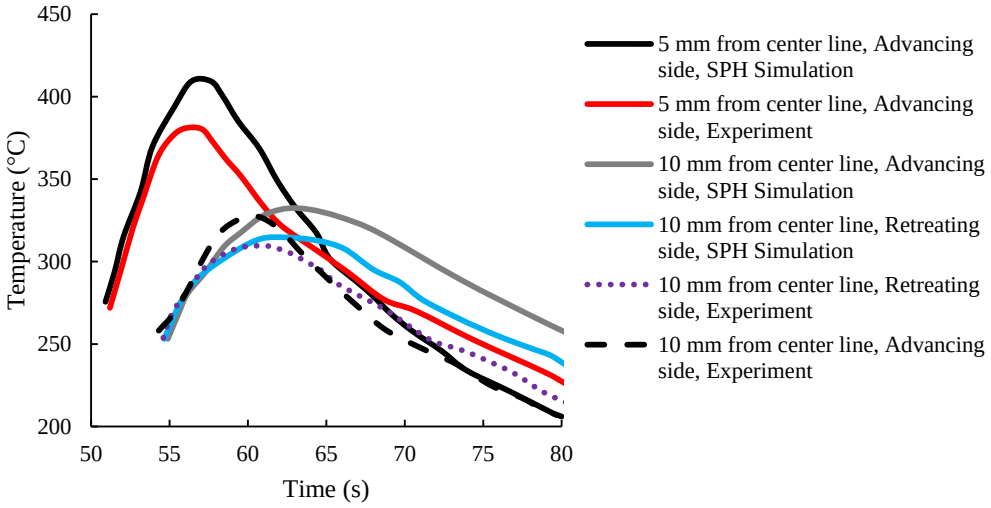


Figure 3. The experimental measurement of the thermal cycles of samples S1 and S3.

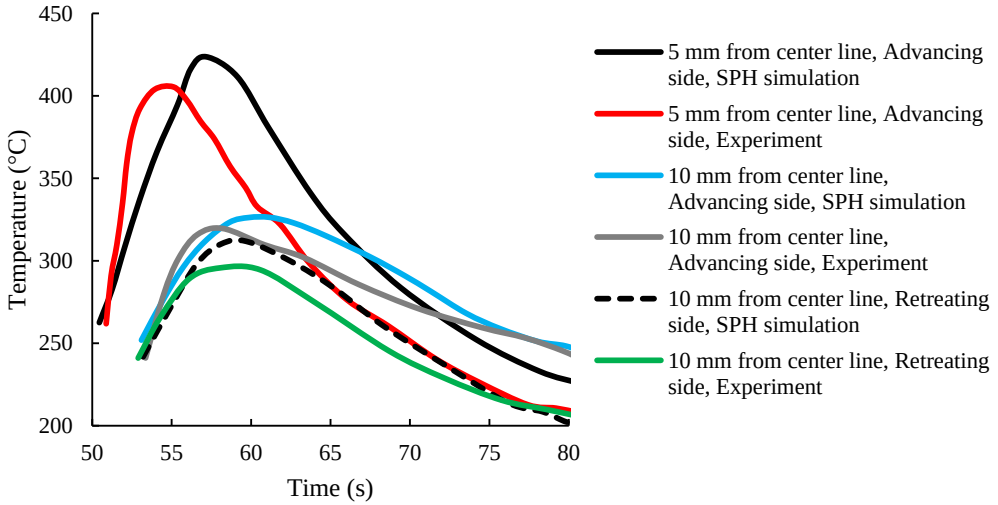
Figure 4 compares the simulation and experimental temperature profiles of samples S2 and S4. The results indicate an acceptable difference between the experimental and simulation data regarding cooling and heating rates and the maximum temperature value. The average temperature difference between the simulation and experimental results was around 25 °C. Several factors may contribute to this difference, including the material properties used in the simulation, measurement error during experimentation, and simplifying assumptions made in the model.

Figure 5 displays the strain rate profile for samples S1 and S3. When the AA6061 alloy is located on the advancing side, the difference in strain rate between the advancing and retreating sides, particularly around the pin, is much greater than when the alloy is placed on the retreating side. This can be attributed to the higher temperature observed on the advancing side (as indicated by the experimental and simulation results) and the lower flow stress of the AA6061 alloy compared to the AA5086 alloy at high temperatures and strain rates [31]. It is worth noting that the material flow is smoother on the AA6061 side, resulting in a more pronounced difference in the strain rate between the two sides. In contrast, when the AA5086 alloy is located on the advancing side, the strain rate distribution between the advancing and retreating sides is almost symmetrical.



(**a**)

Figure 4. *Cont.*



(**b**)

Figure 4. Comparing experiment and simulation results of the thermal cycles of (**a**) sample S2, (**b**) sample S4.

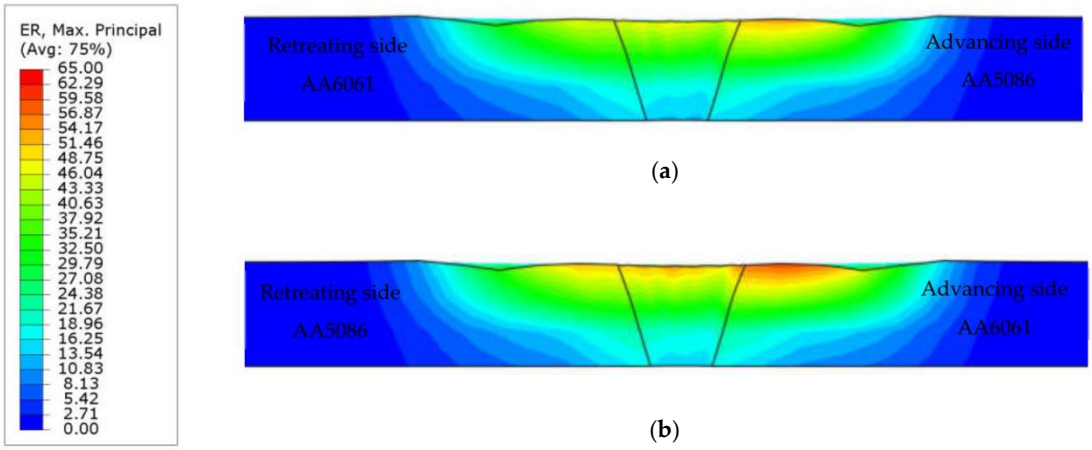


Figure 5. The predicted plastic strain rate of (**a**) sample S1 and (**b**) sample S3.

Figure 6 illustrates the microstructure of the stir zone in different samples, with grain size reported in Table 4. The microstructure in Figure 6 is related to the 1 mm distance from the weld center line at the middle thickness of the AA6061 and AA5086 sheets. In both AA5086 and AA6061, the grain size in the stir zone enlarges with increasing heat input. Furthermore, the grain size of the AA5086 alloy side is generally coarser than that of the AA6061 alloy side. It is found that when the AA5086 alloy is placed on the advancing side, the grain size is larger than when it is positioned on the retreating side. The difference in grain size between different states can be attributed to strain rate and temperature discrepancies. Specifically, when the AA6061 alloy is on the advancing side, both the strain rate and temperature are higher than in the other case. Conversely, when the AA5086 alloy is on the advancing side, the temperature and strain rate on the advancing side are higher than on the retreating side.

Based on these explanations, the difference in grain size can be explained by various mechanisms that contribute to dynamic recrystallization in the stir zone, as mentioned in the review of other studies [32–34]. Temperature and strain rate are two significant factors that influence recrystallization in the stir zone [35]. In addition to these factors, nanometer-sized precipitates in the AA6061 alloy in the stir zone can act as dislocation-locking factors

and delay recrystallization. In contrast, the AA5086 alloy in the stir zone contains larger secondary particles (approximately 0.1 to 0.9 μm in size, see Figure 6). These particles can act as stimulation sources for recrystallization, resulting in faster recrystallization and grain growth in this alloy. The exact recrystallization mechanism during FSW in these alloys is difficult to determine. However, temperature, strain rate, and microscopic studies demonstrate that the coarser equiaxed grains on the AA5086 alloy side compared to the AA6061 alloy side can be attributed to the higher recrystallization and growth rate of the AA5086 alloy.

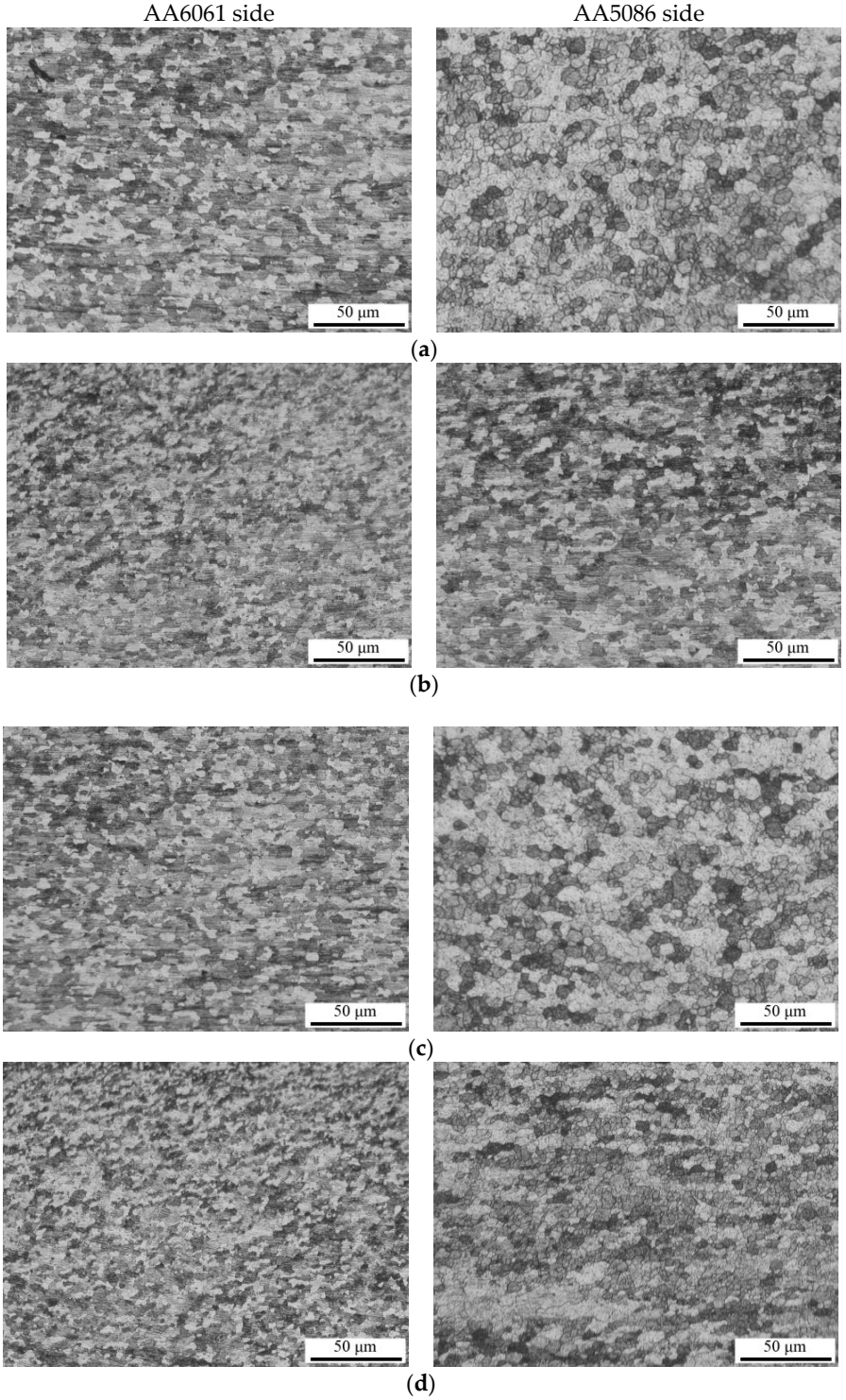
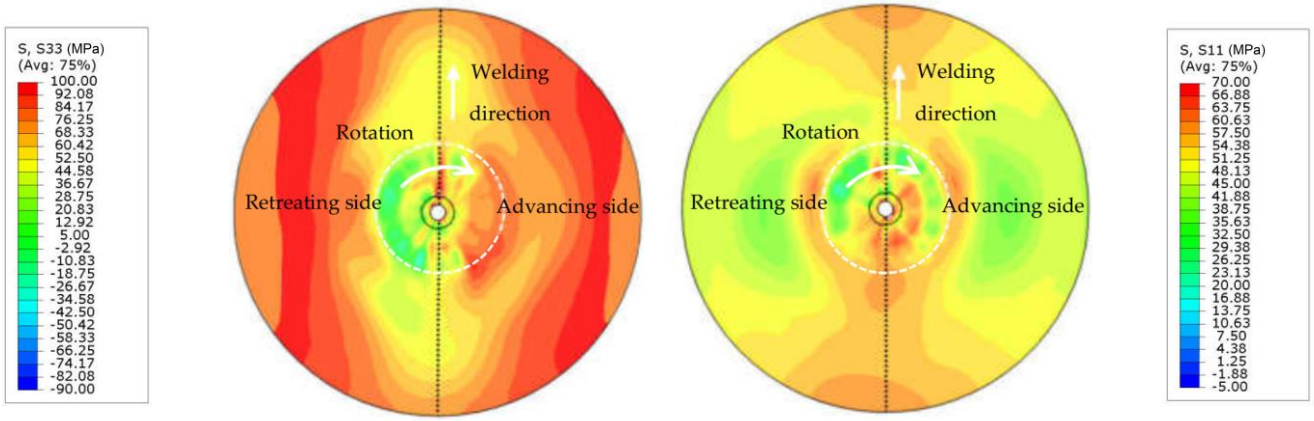


Figure 6. The stir zone grain size of (**a**) sample S1, (**b**) sample S2, (**c**) sample S3, (**d**) sample S4.

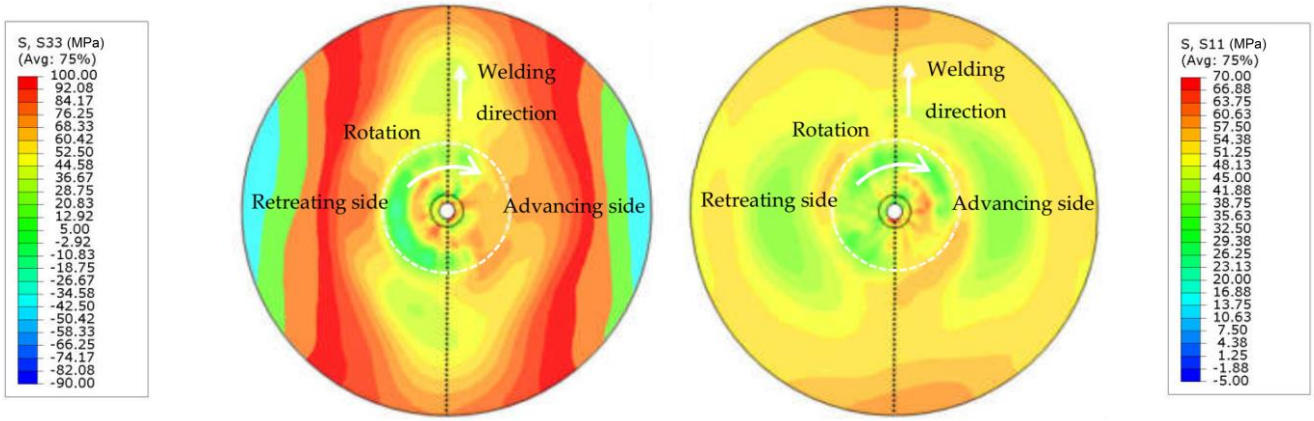
Table 4. The average grain size and maximum predicted temperature of stir zone of different samples.

Sample	AA6061 Side		AA5086 Side	
	Grain Size (μm)	Maximum Predicted Temperature (°C)	Grain Size (μm)	Maximum Predicted Temperature (°C)
S1	9.1	473	10.8	485
S2	6.4	441	7.9	456
S3	8.3	460	10	452
S4	5.9	435	7	423

Figure 7 presents the longitudinal and transverse residual stress profiles of samples S1 and S2 obtained through simulation. The results reveal that residual stress has a tensile nature around the weld line, which changes to compressive away from the joint line. The asymmetric distribution of residual stress in the studied domain can be attributed to the asymmetric nature of the FSW process and the distinct properties of the AA5086 and AA6061 alloys. Increasing the traverse speed at a constant rotational speed (Samples S1 and S2) reduces the area under tensile stress. In other words, an increase in heat input per unit length of the weld increases the maximum tensile residual stress and the area it affects. Based on the welding parameters, the transverse residual stress value is approximately 40 to 60% of the longitudinal residual stress value.



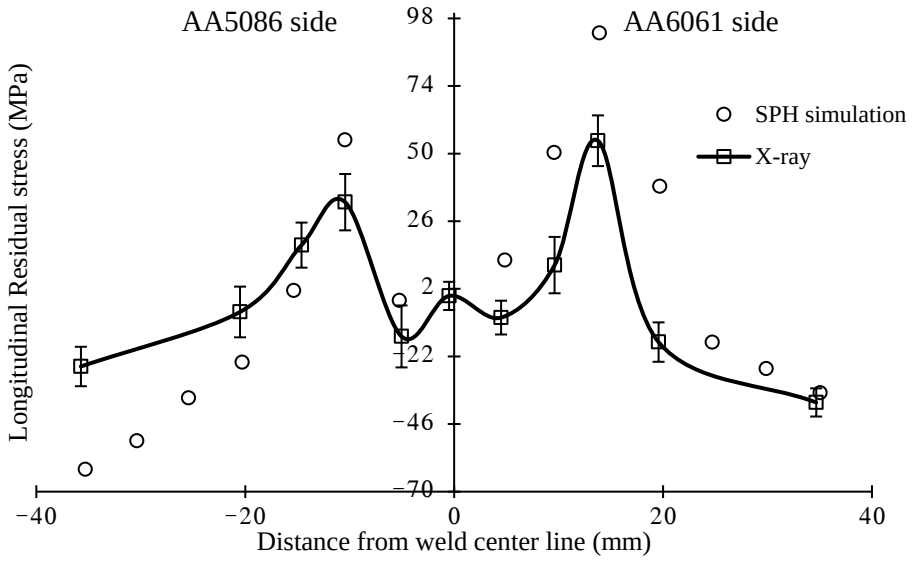
(**a**)



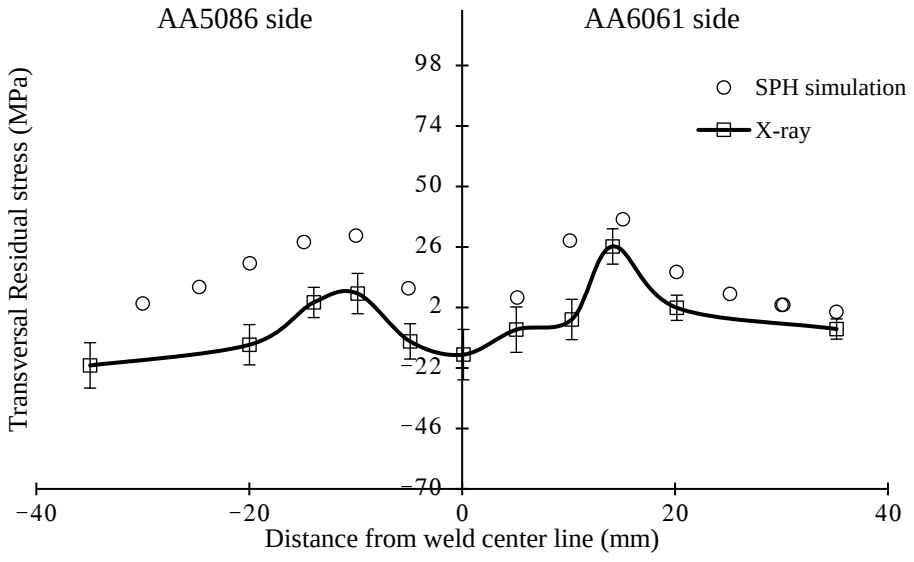
(**b**)

Figure 7. The longitudinal and transversal residual stresses of (**a**) sample S1, and (**b**) sample S2. The tool position is marked by the white dashed line.

Figure 8 compares the longitudinal and transverse residual stress results of sample S3 obtained from the simulation and X-ray methods. As observed, the trend of longitudinal and transverse stress changes is the same in both methods, but the results have minor differences. These differences can be attributed to factors such as the simulation domain and the input properties of the materials in the model. It is noteworthy that the model used in this study only considers a part of the workpiece and does not account for constraints throughout the entire workpiece. Despite this limitation, efforts were made to consider conditions as similar to the experimental work as possible.



(**a**)



(**b**)

Figure 8. Comparing the predicted and measured residual stress of sample S3: (**a**) longitudinal residual stress, (**b**) transversal residual stress.

Figure 9 shows the horizontal hardness profile across the joints measured at a depth of 2 mm from the root face after FSW, where the AA5086 and AA6061 base metals show Vickers hardnesses of about 62HV and 101HV, respectively. On the AA5086 side, because of recrystallization and the generation of fine grains in the weld nugget, the micro-hardness

is higher than the base metal. On the other hand, the partial dissolving of precipitates and the potential for subsequent natural aging of AA606 result in complicated variations in the hardness profile of the welded samples. As shown in Figure 9, on the AA6061 side, an abrupt decrease in hardness can be observed. Partial dissolution of the hardening particles β'' and β' occurs within the thermo-mechanically affected zone (TMAZ) and the stir zone (SZ) of AA6061 during welding owing to the imposed heat input and severe plastic deformation. However, the hardness in the above regions increases during subsequent natural aging, especially in the stir zone, where the material experiences greater plastic strains and higher temperatures.

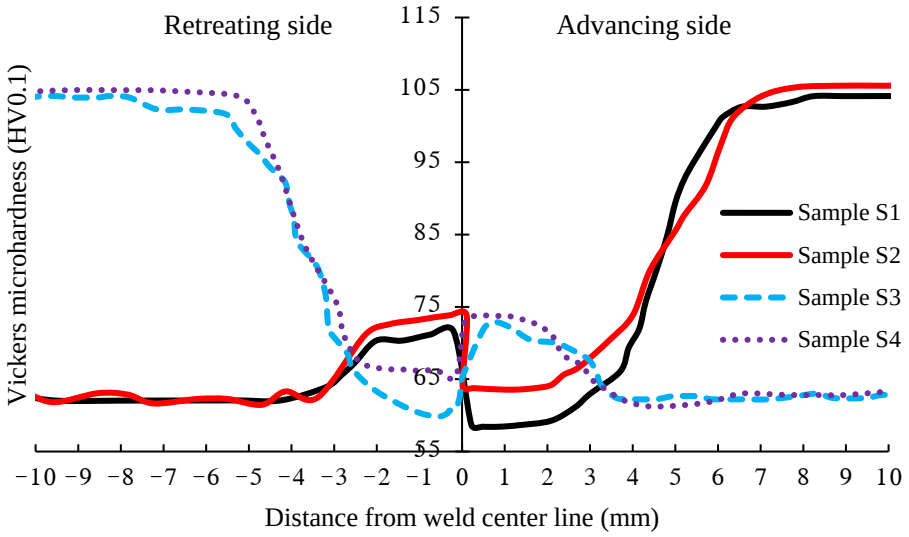


Figure 9. Micro-hardness profile of different samples.

5. Conclusions

Using smoothed-particle hydrodynamics methods to predict dissimilar FSW of AA5086 and AA6061 aluminum alloys has yielded several key findings. These include:

(1) The presented model can estimate temperature changes and residual stresses in dissimilar FSW of the AA5086 and AA6061 aluminum alloys with a maximum error of 14% and 11%, respectively.

(2) Both simulation and experimental investigations reveal that changing the position of the AA6061 aluminum alloy on the advancing or retreating side significantly affects the thermal profile. Specifically, when the AA6061 alloy is on the retreating side, the temperature profile becomes more symmetrical than its previous state.

(3) The strain rate distribution between the advancing and retreating sides is almost symmetrical when the AA5086 alloy is on the advancing side.
The strain rate results indicate that when the AA6061 alloy is on the advancing side, both the strain rate and temperature are higher than in the other case.

(4) When the AA5086 alloy is positioned on the advancing side, the maximum temperature and strain rate on the advancing side are higher than on the retreating side.

(5) Using the same welding parameters, when the AA6061 alloy is located on the advancing side, the difference in strain rate between the advancing and retreating sides is around 15–18% greater than when the alloy is placed on the retreating side.

(6) On the AA5086 side, because of recrystallization and generation of fine grains in the weld nugget, the micro-hardness is higher than the base metal. On the other hand, the partial dissolving of precipitates on the AA6061 side leads to an abrupt decrease in hardness.

(7) Compared to base metals, by increasing the traverse speed from 10 to 15 cm/min at 900 rpm, the hardness of the stir zone on the AA5086 and AA6061 sides increases and decreases by 16 and 35%, respectively.

Funding: This research received no external funding.

Data Availability Statement: Data will be made available on request.

Conflicts of Interest: The author declares no conflict of interest.

References

1. Babalola, S.A.; Dutta, S.; Murmu, N.C.; Akinnuli, B.O. In-situ process reliability monitoring strategy for friction stir welding machine. *Mater. Today Proc.* **2022**, *66*, 3883–3889. [CrossRef]
2. Gopan, V.; Wins, K.L.D.; Surendran, A. Innovative potential of additive friction stir deposition among current laser based metal additive manufacturing processes: A review. *CIRP J. Manuf. Sci. Technol.* **2021**, *32*, 228–248. [CrossRef]
3. Ahmed, M.M.Z.; Seleman, M.M.E.-S.; Fydrych, D.; Çam, G. Friction Stir Welding of Aluminum in the Aerospace Industry: The Current Progress and State-of-the-Art Review. *Materials* **2023**, *16*, 2971. [CrossRef] [PubMed]
4. Xie, Y.; Society, A.W.; Meng, X.; Huang, Y. Entire-process simulation of friction stir welding—Part 1: Experiments and simulation. *Weld. J.* **2022**, *101*, 144–159. [CrossRef]
5. Aval, H.J.; Serajzadeh, S.; Kokabi, A.H. Thermo-mechanical and microstructural issues in dissimilar friction stir welding of AA5086–AA6061. *J. Mater. Sci.* **2011**, *46*, 3258–3268. [CrossRef]
6. Aval, H.J.; Serajzadeh, S.; Kokabi, A.H. The influence of tool geometry on the thermo-mechanical and microstructural behaviour in friction stir welding of AA5086. *Proc. Inst. Mech. Eng. Part C J. Mech. Eng. Sci.* **2010**, *225*, 1–16. [CrossRef]
7. Maniscalco, J.; Elmustafa, A.A.; Bhukya, S.; Wu, Z. Numerical Simulation of the Donor-Assisted Stir Material for Friction Stir Welding of Aluminum Alloys and Carbon Steel. *Metals* **2023**, *13*, 164. [CrossRef]
8. Hossfeld, M. Modeling Friction Stir Welding: On Prediction and Numerical Tool Development. *Metals* **2022**, *12*, 1432. [CrossRef]
9. Janga, V.S.R.; Awang, M. Influence of Plunge Depth on Temperatures and Material Flow Behavior in Refill Friction Stir Spot Welding of Thin AA7075-T6 Sheets: A Numerical Study. *Metals* **2022**, *12*, 927. [CrossRef]
10. Iqbal, P.; Jain, R.; Pal, S.K.; Mandal, P. Numerical modelling of friction stir welding of pipes: Effect of tool shoulder on mechanical property and metallurgical characterization. *J. Manuf. Process.* **2022**, *79*, 326–339. [CrossRef]
11. Su, H.; Wu, C. Numerical simulation for the optimization of polygonal pin profiles in friction stir welding of aluminum. *Acta Met. Sin. (Engl. Lett.)* **2021**, *34*, 1065–1078. [CrossRef]
12. Nandan, R.; Roy, G.G.; Debroy, T. Numerical simulation of three-dimensional heat transfer and plastic flow during friction stir welding. *Met. Mater. Trans. A* **2006**, *37*, 1247–1259. [CrossRef]
13. Arora, A.; Zhang, Z.; De, A.; DebRoy, T. Strains and strain rates during friction stir welding. *Scr. Mater.* **2009**, *61*, 863–866. [CrossRef]
14. Chen, G.; Feng, Z.; Zhu, Y.; Shi, Q. An alternative frictional boundary condition for computational fluid dynamics simulation of friction stir welding. *J. Mater. Eng. Perform.* **2016**, *25*, 4016–4023. [CrossRef]
15. Shi, L.; Wu, C.S.; Liu, H.J. The effect of the welding parameters and tool size on the thermal process and tool torque in reverse dual-rotation friction stir welding. *Int. J. Mach. Tools Manuf.* **2015**, *91*, 1–11. [CrossRef]
16. Chen, G.; Li, H.; Wang, G.; Guo, Z.; Zhang, S.; Dai, Q.; Wang, X.; Zhang, G.; Shi, Q. Effects of pin thread on the in-process material flow behavior during friction stir welding: A computational fluid dynamics study. *Int. J. Mach. Tools Manuf.* **2018**, *124*, 12–21. [CrossRef]
17. Sun, Z.; Wu, C. Influence of tool thread pitch on material flow and thermal process in friction stir welding. *J. Mater. Process. Technol.* **2020**, *275*, 116281. [CrossRef]
18. Zhang, S.; Shi, Q.; Liu, Q.; Xie, R.; Zhang, G.; Chen, G. Effects of tool tilt angle on the in-process heat transfer and mass transfer during friction stir welding. *Int. J. Heat Mass Transf.* **2018**, *125*, 32–42. [CrossRef]
19. Yang, C.; Wu, C.; Lv, X. Numerical analysis of mass transfer and material mixing in friction stir welding of aluminum/magnesium alloys. *J. Manuf. Process.* **2018**, *32*, 380–394. [CrossRef]
20. Yang, C.-Y. Inverse determination of heat input during the friction stir welding process. *Int. J. Heat Mass Transf.* **2014**, *76*, 411–418. [CrossRef]
21. Xiao, Y.; Zhan, H.; Gu, Y.; Li, Q. Modeling heat transfer during friction stir welding using a meshless particle method. *Int. J. Heat Mass Transf.* **2017**, *104*, 288–300. [CrossRef]
22. Wang, X.; Gao, Y.; Liu, X.; McDonnell, M.; Feng, Z. Tool-workpiece stick-slip conditions and their effects on torque and heat generation rate in the friction stir welding. *Acta Mater.* **2021**, *213*, 116969. [CrossRef]
23. Ahmed, M.M.Z.; Habba, M.I.A.; Jouini, N.; Alzahrani, B.; Seleman, M.M.E.-S.; El-Nikhaily, A. Bobbin tool friction stir welding of aluminum using different tool pin geometries: Mathematical models for the heat generation. *Metals* **2021**, *11*, 438. [CrossRef]
24. Zhao, W.; Wu, C.; Su, H. Numerical investigation of heat generation and plastic deformation in ultrasonic assisted friction stir welding. *J. Manuf. Process.* **2020**, *56*, 967–980. [CrossRef]

25. Singh, B.; Sharma, S.; Kumar, V.; Maheshwari, K.; Singhal, P. A Review on Heat Generation and Temperature Distribution Models in Friction stir Welding (FSW). In *IOP Conference Series: Materials Science and Engineering*; IOP Publishing: Bristol, UK, 2021; p. 012080.
26. Kim, D.; Badarinarayan, H.; Kim, J.H.; Kim, C.; Okamoto, K.; Wagoner, R.; Chung, K. Numerical simulation of friction stir butt welding process for AA5083-H18 sheets. *Eur. J. Mech. A/Solids* **2010**, *29*, 204–215. [CrossRef]
27. Li, S.; Sui, J.; Ding, F.; Wu, S.; Chen, W.; Wang, C. Optimization of Milling Aluminum Alloy 6061-T6 using Modified Johnson-Cook Model. *Simul. Model. Pract. Theory* **2021**, *111*, 102330. [CrossRef]
28. Abdulhamid, H.; Kolopp, A.; Bouvet, C.; Rivallant, S. Experimental and numerical study of AA5086-H111 aluminum plates subjected to impact. *Int. J. Impact Eng.* **2013**, *51*, 1–12. [CrossRef]
29. Sirigiri, V.K.R.; Gudiga, V.Y.; Gattu, U.S.; Suneesh, G.; Buddaraju, K.M. A review on Johnson Cook material model. *Mater. Today Proc.* **2022**, *62*, 3450–3456. [CrossRef]
30. Bal, B.; Karaveli, K.K.; Cetin, B.; Gumus, B. The precise determination of the johnson–cook material and damage model parameters and mechanical properties of an aluminum 7068-t651 alloy. *J. Eng. Mater. Technol.* **2019**, *141*, 041001. [CrossRef]
31. Prasad, Y.; Rao, K.; Sasidhar, S. *Hot Working Guide: A Compendium of Processing Maps*; ASM International: Materials Park, OH, USA, 2015.
32. Yu, P.; Wu, C.; Shi, L. Analysis and characterization of dynamic recrystallization and grain structure evolution in friction stir welding of aluminum plates. *Acta Mater.* **2021**, *207*, 116692. [CrossRef]
33. Dong, J.; Zhang, D.; Luo, X.; Zhang, W.; Zhang, W.; Qiu, C. EBSD study of underwater friction stir welded AA7003-T4 and AA6060-T4 dissimilar joint. *J. Mater. Res. Technol.* **2020**, *9*, 4309–4318. [CrossRef]
34. Xie, J.; Chen, X.; Cao, Y.; Sun, Y.; Huang, G.; Liu, Q. The heterogeneity of dynamic recrystallization and texture evolution in stirring zone of Al-Mg-Sc alloy. *Mater. Charact.* **2022**, *191*, 112092. [CrossRef]
35. Humphreys, F.; Hatherly, M. *Recrystallization and Related Annealing Phenomena*; Elsevier: Amsterdam, The Netherlands, 2012.

Disclaimer/Publisher's Note: The statements, opinions and data contained in all publications are solely those of the individual author(s) and contributor(s) and not of MDPI and/or the editor(s). MDPI and/or the editor(s) disclaim responsibility for any injury to people or property resulting from any ideas, methods, instructions or products referred to in the content.